Adrenergic nerve degeneration in bone marrow drives aging of the hematopoietic stem cell niche

Maria Maryanovich[1,2], **Ali H. Zahalka**[1,2,*], **Halley Pierce**[1,2,*], **Sandra Pinho**[1,2,3], **Fumio Nakahara**[1,2], **Noboru Asada**[1,2,#], **Qiaozhi Wei**[1,2], **Xizhe Wang**[1,2], **Paul Ciero**[1,2], **Jianing Xu**[4], **Avigdor Leftin**[5], and **Paul S. Frenette**[1,2,3]

[1]Ruth L. and David S. Gottesman Institute for Stem Cell and Regenerative Medicine Research, Albert Einstein College of Medicine, New York, NY, USA

[2]Department of Cell Biology, Albert Einstein College of Medicine, Bronx, New York, NY, USA

[3]Department of Medicine, Albert Einstein College of Medicine, Bronx, New York, NY,, USA

[4]Human Oncology and Pathogenesis Program, Memorial Sloan Kettering Cancer Center, New York, NY,, USA

[5]Department of Medical Physics, Memorial Sloan Kettering Cancer Center, New York, NY, USA

Abstract

Aging of hematopoietic stem cells (HSCs) is associated with a decline in their regenerative capacity and multi-lineage differentiation potential, contributing to the development of blood disorders. The bone marrow microenvironment has recently been suggested to influence HSC aging, but the underlying mechanisms remain largely unknown. Here, we show that HSC aging critically depends on bone marrow innervation by the sympathetic nervous system (SNS), as loss of SNS nerves or adrenoreceptor β3 (ADRβ3) signaling in the bone marrow microenvironment of young mice led to premature HSC aging, as evidenced by appearance of HSC phenotypes reminiscent of physiological aging. Strikingly, supplementation of a sympathomimetic acting selectively on ADRβ3 to old mice significantly rejuvenated the *in vivo* function of aged HSCs, suggesting that the preservation or restitution of bone marrow SNS innervation during aging may hold the potential for new HSC rejuvenation strategies.

Corresponding author: Paul S. Frenette, paul.frenette@einstein.yu.edu.
*These authors contributed equally to this work.
#Current address: Okayama University Hospital, Department of Hematology and Oncology, Okayama, Japan
Correspondence and requests for materials should be addressed to P.S.F. (paul.frenette@einstein.yu.edu).

Mammalian aging can be described as time-dependent functional decline in physiologic homeostasis of many tissues, leading to increased risk of cardio-vascular diseases, neurodegenerative diseases, cancer and diabetes[1]. One of the major causes for age-associated tissue attrition is a functional decline in tissue-specific stem cells[2]. In the hematopoietic system, life-long blood production depends on the ability of hematopoietic stem cells (HSCs) to self-renew, differentiate, and form all blood cell lineages[3]. Aging of the blood system is associated with myeloproliferation, immune senescence and anemia, attributed to age-dependent decline in HSC function due to loss of regenerative potential and myeloid-biased differentiation[4]. Studies have identified multiple HSC intrinsic factors that regulate their aging. Among these are mechanisms controlling HSC metabolism (autophagy, mitochondrial dysfunction and nutrient sensing)[5–9], replicative stress[10] and DNA damage and repair responses[11–14]. It has also been suggested that alterations in the epigenetic landscape and cell polarity may drive HSC aging manifestations[15–17]. Recent studies indicate that aging is also associated with drastic changes to the bone marrow microenvironment and suggest that factors extrinsic to HSCs, may promote their aged phenotype[18–22].

HSCs reside in a specialized microenvironment in the bone marrow (also referred to as niche), which represents a critical regulatory unit essential to maintain healthy hematopoiesis[23]. HSC niches have recently been identified as perivascular units[23], where subsets of quiescent HSCs are closely associated with arteriolar perivascular Nestin-GFP[+] mesenchymal stem cells (MSCs), glial fibrillary acidic protein (GFAP)-expressing Schwann cells from adrenergic nerves, and megakaryocytes[18,24–30]. The sympathetic nervous system (SNS) represents an important regulatory component of the HSC niche, orchestrating release of adrenergic neurotransmitter into the microenvironment in a circadian manner[31–33]. These autonomic signals regulate the proliferative state of Nestin-GFP[+] MSCs, HSC mobilization, and the hematopoietic regenerative capacity following genotoxic stress[34–36]. Here, we have evaluated the impact of aging on the bone marrow microenvironment and have uncovered, unexpectedly, that the loss of sympathetic nerve fibers around arteriolar niches, was a potent driver of hematopoietic aging.

RESULTS

Aging-related alterations of HSC niches

To define how aging impacts HSC niches, we compared the bone marrow (BM) vascular architecture by whole-mount 3D confocal fluorescence imaging[25] of young (8–10-week-old) and old (20–24-month-old) C57BL/6 mice and *Nestin-GFP* mice, in which GFP marks putative HSC niche cells[24]. Nestin-GFP^{+} niche cells can be divided into two distinct subpopulations based on GFP expression: Nestin-GFP^{bright} cells are exclusively found along arteries, while the more abundant Nestin-GFP[dim] population is largely associated with sinusoids[25]. Consistent with a recent study describing aging-related alterations in BM[18], we found that aging imposed drastic remodeling of bone marrow vascular architecture (Fig. 1a), as evidenced by an overall increase in vascular density (Fig. 1b) and apparent deterioration of arteriolar structures marked by significant shortening of Nestin-GFP[bright] arteriole segments (Fig. 1c) and loss of α-smooth muscle actin positive (α-SMA^{+}) density (Fig. 1d).

FACS analyses confirmed the imaging results and revealed that the absolute number of CD45$^-$ Ter119$^-$ CD31^{high} total endothelial cells (ECs) were significantly increased while CD45$^-$ Ter119$^-$ CD31^{high} Sca-1^{high} arteriolar ECs were reduced in aged mice compared to young BM counterparts (Supplementary Fig. 1a).

Imaging of the rare Nestin-GFP^{bright} population revealed a significant expansion of these cells in old femurs (Fig. 1e), which was further confirmed by FACS analysis, demonstrating a specific expansion of Nestin-GFP^{bright} cells with age, without significant changes in the sinusoidal Nestin-GFP^{dim} population (Fig. 1f and Supplementary Fig. 1b). Interestingly, expanded niche cells were distributed away from endosteal region, converging significantly closer to the central vein (Supplementary Fig. 1c–d). However, the frequency of Nestin-GFP$^+$ MSCs from compact bones were significantly reduced and had a lower colony-forming capacity in culture (Supplementary Fig. 1e–f), indicating differential aging manifestations between bone and marrow MSCs.

We and others have recently reported that subsets of quiescent HSCs are significantly associated with arterioles and megakaryocytes (Mk)[25,27,28,37]. To assess the relationship between HSCs with niche structures during aging, we imaged endogenous CD150$^+$ CD48$^-$ CD41$^-$ Lineage$^-$ HSCs in whole-mount sterna from young and old mice. We found that HSCs in old mice were distributed significantly away from either niche structure compared to young animals (Fig. 1g; Supplementary Fig. 2a) and sometimes found in clusters, away from arterioles or Mk (Fig. 1g; arrow). The loss of association with Mk was observed despite their overall increased numbers in the bone marrow of old mice (Supplementary Fig. 2b–c), with increased numbers of megakaryocyte progenitors (MkP) and age-associated augmentation of platelet counts (Supplementary Fig. 2d–e). These results indicate that aging induces remodeling of HSC niches, associated with attrition of arteriolar structures, expansion of total vascular density and expansion of Nestin-GFP^{bright} MSCs and megakaryocytes leading to redistribution of old HSCs away from their putative niches.

Aging induces the loss of niche-associated adrenergic nerves

The observed arteriolar attrition in old femoral bone marrow (Fig. 1a–c and[18]) suggested that aging may compromise SNS innervation, as these nerves are tightly associated with arterioles[23,25] and are reported to be lost in hematological malignancies[38,39]. Staining for tyrosine hydroxylase positive (TH$^+$) adrenergic nerve fibers revealed a dramatic overall reduction in nerve density in old compared to young femurs (Fig. 2a–b), and also a significant loss of TH$^+$ nerves per Nestin-GFP^{bright} arteriole (Fig. 2c). Staining of young and old femurs with the pan-neuronal marker β-III tubulin confirmed that aging induced a dramatic loss of bone marrow innervation (Fig. 2d–e). To evaluate the possibility of neural dysfunction, we assessed the number of synaptic contacts between nerves and blood vessels by staining for synaptophysin (syp)[40]. In young mice, the staining pattern of synaptophysin exhibited a spiral-like pattern (similar to staining with TH; Fig. 2c) and highly overlapped with β-III Tubulin staining. However, upon aging, the number of syp$^+$ synapses were significantly reduced (Fig. 2f), suggesting a reduction in synapse density per nerve. The loss of SNS was not generalized during aging because the nerve density in the aging prostate, an organ highly innervated by the SNS[41], was not significantly altered compared to young mice

(Supplementary Fig. 3a). Additionally, the expression of nerve growth factor (*Ngf*), a major neurotrophin for SNS nerves[42], which is selectively expressed by MSCs in bone marrow, was significantly reduced upon aging (Supplementary Fig. 3b). As SNS nerves regulate HSC egress in a circadian manner[24,31,32,34], we evaluated whether the age-associated bone marrow SNS neuropathy had a functional consequence for circadian rhythms of circulating progenitors. Whereas the number of phenotypic (Lin⁻ Sca-1⁺ c-Kit⁺; LSK) or functional (colony-forming units in culture; CFU-C) progenitors oscillated in a circadian manner in the blood of young mice, the oscillations of blood progenitors were ablated in old mice (Fig. 3a–b). These changes were matched by inverse oscillations of HSC retention factor *Cxcl12* mRNA levels in CD45⁻ Ter119⁻ CD31⁻ CD51⁺ PDGFRα⁺ MSCs[43] of young mice while no significant circadian changes were detected in old MSCs (Fig. 3c). Thus, these results suggest that the aging HSC niche is associated with the profound loss of functional SNS nerves.

Aging expands bone marrow MSCs with reduced HSC maintenance capacity

Our previous studies have revealed that CD45⁻ Ter119⁻ CD31⁻ CD51⁺ PDGFRα⁺ cells highly overlap with the Nestin-GFP⁺ population, and contain most MSC and HSC-maintaining activity[43]. Consistent with the notion that SNS nerves negatively regulated bone marrow MSC proliferation[36], and that aging caused bone marrow SNS neuropathy, we found that, similar to Nestin-GFP^bright stromal cells (Fig. 1e–f), CD45⁻ Ter119⁻ CD31⁻ CD51⁺ PDGFRα⁺ stromal cells obtained from old mice were expanded (Fig. 3d and Supplementary Fig. 4b) and were significantly more proliferative compared to young counterparts, as determined by Ki-67 expression (Fig. 3e). Although aging significantly increased the overall BM cellularity (Supplementary Fig. 4a), we did not detect any changes in the absolute numbers and frequency of CD45⁻ Ter119⁻ CD31⁻ CD51⁻ PDGFRα⁻ non-MSC cells (Supplementary Fig. 4c), suggesting specificity in MSC expansion. MSCs derived from old mice exhibited lower clonogenic potential *in vitro* (Fig. 3f–g) with reduced osteogenic potential (Supplementary Fig. 4d–e) and enhanced *in vivo* adipogenic differentiation, following sublethal irradiation, as determined by Perilipin⁺ areas (Supplementary Fig. 4f), in line with previous reports[44]. In addition, sorted MSCs from old mice expressed lower mRNA levels of the canonical niche factors, *Cxcl12*, *Scf* and *Angpt1* (Fig. 3h), suggesting a reduced HSC maintenance activity. These results thus indicate that the loss of SNS nerves may have functional consequences on MSC function during niche aging.

To define better the onset of HSC niche aging, we evaluated *Nestin-GFP* bone marrow at 2, 8 and 12 months of age. These analyses revealed that the loss of TH⁺ nerves and reduced arteriolar segment length, as well as the increased numbers of Nestin-GFP^bright cells or CD45⁻ Ter119⁻ CD31⁻ CD51⁺ PDGFRα⁺ MSCs were already apparent at 8 months of age, whereas the changes in overall vascular density were not statistically significant at this time (Supplementary Figs. 1a, 4b, and 5a–e). These findings are consistent with a recent report documenting the emergence of aging phenotypes, such as HSC expansion and lymphoid dysfunction, from 8 months of age[45]. We also confirmed that the frequency and absolute numbers of phenotypic HSCs (Lineage⁻ CD48⁻ c-Kit⁺ Sca-1⁺ CD150⁺) were significantly increased at 8 months of age, and found that the HSC population was significantly redistributed away from arterioles at this age (Supplementary Fig. 5f–g). Thus, SNS

neuropathy in bone marrow is an early hallmark of the aging HSC niche, apparent in 8-month-old adult mice and concurrent with HSC aging.

Loss of SNS-nerves induces premature niche and HSC aging

The loss of sympathetic innervation could merely accompany the vascular remodeling and aging-associated alterations in hematopoiesis, or alternatively, it could represent a driver of the aging process. To investigate this critical issue, we unilaterally denervated the hind limb of young *Nestin-GFP* or C57BL/6 mice by surgical transection of the femoral and sciatic nerves, as previously described[32,46,47], while the contralateral limb was sham-operated (Fig. 4a). This surgical strategy, of nerve transaction in the abdominal area close to their origin in the spinal column and prior to neural branching, produced a complete loss of TH$^+$ nerves, specifically in the denervated femur (Supplementary Fig. 6) and thus enabled us to compare the impact of neural input on the aging phenotype in the same animal. As we have previously reported, acute bone marrow denervation using 6-Hydoxydopamine (6OHDA), 7 days post denervation, did not result in a detectable HSC phenotype at steady state[36]. Thus, to evaluate whether SNS nerves play a role in the aging process, we denervated mice in their youth (2 months old) and sacrificed them at 4 months post-surgery (6 months of age), to avoid extending the age over 8 months when aging phenotypes are apparent (Supplementary Figs. 1a, 4a–c and 5a–g and[45]).

Strikingly, we found that phenotypic HSCs were more proliferative (Supplementary Fig. 7a) and expanded in the denervated, but not in the nerve-intact femurs (Fig. 4b), with specific expansion of myeloid-biased CD41$^+$ HSCs (Supplementary Fig. 7b) a phenotype reminiscent of chronologically aged HSCs[48]. Competitive repopulation assays using whole bone marrow (WBM) revealed increased overall donor-derived repopulation activity in the denervated bone, compared to nerve-intact bone, with myeloid-biased differentiation 4 months following transplantation and increased engraftment of donor HSCs (Supplementary Fig. 7c–i), which is also similar to the previously reported competitive advantage of WBM transplantation from old mice[49,50]. Using a separate cohort of mice, we also evaluated the competitive repopulating capacity of 200 sorted HSCs from denervated and nerve-intact bone marrow to assess their self-renewal and differentiation potential. These results revealed dramatic reductions of engraftment capacity and lymphoid cell production of HSCs harvested from denervated (referred to as denervated HSCs), compared to nerve-intact bone marrow, which was maintained upon secondary transplantation (Fig. 4c–d). To confirm further that unilateral surgical denervation led to aging of HSCs, we evaluated comparatively the polarity and DNA damage of denervated and nerve-intact HSCs as aging has previously been suggested to be associated with a loss of polarity and increased DNA damage in HSCs[10,17]. Indeed, immunofluorescence analysis of sorted HSCs from either young, old, sham or denervated femurs revealed that Cdc42 and Tubulin polarity was significantly altered, and γ-H2AX foci formation was significantly increased in denervated HSCs compared to sham control, reaching frequencies similar to old HSCs (Fig. 4e–f, Supplementary Fig. 8a–c). These data suggest that the denervation leads to a premature aging-like HSC phenotype, with expansion of myeloid-biased HSCs with reduced long-term self-renewal capacity.

To determine the impact of denervation on aging of the HSC niche, we evaluated the vascular structures and their associated stromal cells by whole-mount immunofluorescence imaging and FACS. Remarkably, denervation induced a remodeling of the bone marrow microenvironment reminiscent of that of aged mice, characterized with arteriolar segment shortening (Fig. 4g) and loss of α-SMA^{+} cells (Supplementary Fig. 8d). In addition, surgical bone marrow denervation in young mice led to augmentations in bone marrow cellularity (Supplementary Fig. 8e), numbers of CD31^{high} total ECs (Supplementary Fig. 8f) and CD45^{−} Ter119^{−} CD31^{−} CD51^{+} PDGFRα^{+} MSCs (Fig. 4h) that exhibit reduced clonogenic potential (Fig. 4i), as observed in chronologically aged mice. Moreover, MSCs harvested from denervated bones exhibited reduced expression of major HSC maintenance factors (Fig. 4j) and diminished osteogenic potential (Supplementary Fig. 8g), compared to those harvested from nerve-intact contralateral bone. These data strongly indicate that the premature loss of SNS nerves in young mice can drive the emergence of an aged HSC niche.

Because unilateral surgical denervation results in complete immobility of the denervated limb, it could be argued that the aging-like HSC and niche phenotypes could be an indirect effect of reduced limb mobility on the skeleton or to collateral denervation of non-hematopoietic organs (e.g. muscle). To evaluate this possibility, we performed a musculo-cutaneous denervation of the hindlimb by transecting the sciatic nerve distal to the spinal cord close to the sciatic notch, and the femoral nerve distal to the spinal cord, as previously reported not to directly affect bone and marrow homeostasis[51,52]. As expected, hindlimb musculo-cutaneous denervation did not eliminate sympathetic nerves in denervated femurs and did not induce any aging-like HSC and niche phenotypes 4 months after surgery (Supplementary Fig. 9a–c), confirming that aging-like phenotypes observed in denervated femurs are directly related to bone marrow denervation.

HSC aging depends on niche-derived ADRβ3 signals

SNS nerves locally deliver noradrenaline as its major neurotransmitter targeting β2 (ADRβ2) and β3 (ADRβ3) adrenergic receptors in the bone marrow microenvironment[32,34,35]. While *Adrb2* is broadly expressed in both hematopoietic and non-hematopoietic compartments, *Adrb3* expression is restricted to the stroma and does not change with aging (our analyses of published HSC[53] and stromal[54] RNAseq datasets and Supplementary Fig. 10a–c). We thus tested whether the administration of sympathomimetics, an ADRβ2-selective agonist (Clenbuterol) or an ADRβ3-selective agonist (BRL37344) could rejuvenate the HSC niche and HSCs of old mice. Continuous sympathomimetic delivery was achieved by serial sub-cutaneous implantations of Alzet osmotic pumps in aged C57BL/6 animals to achieve drug delivery over 12 weeks. As control, both young and old mice received pumps filled with saline (Supplementary Fig. 11a). Treatment of old mice with either sympathomimetic was well tolerated and did not produce any hematological toxicity as determined by stable blood counts at the termination of drug delivery (Supplementary Table 1). Remarkably, the administration of either sympathomimetic lowered the absolute numbers and frequencies of MSCs and ECs to levels similar to those observed in young mice, without detectable alterations in bone marrow cellularity (Fig. 5a and Supplementary Fig. 11b–e), suggesting a potential for niche rejuvenation. Additionally, treatment of old mice with either β-adrenergic-selective

sympathomimetic significantly reduced the number of phenotypic HSCs (Fig. 5b and Supplementary Fig. 11f). To test the rejuvenation potential of these agents on HSC function, we then competitively transplanted sorted HSCs obtained from these treated mice. While ADRβ2 agonist treatment did not improve old HSC engraftment and contribution to the lymphoid lineage, treatment with the ADRβ3 agonist markedly increased donor chimerism to near normal levels in peripheral blood and bone marrow 5 months following transplantation (Fig. 5c). In addition, ADRβ3 agonist significantly improved multi-lineage cell production and HSC engraftment (Fig. 5c and Supplementary Fig. 11g–j). The functional rejuvenation of old HSCs by ADRβ3 agonist treatment was also evident following secondary bone marrow transplantation, in which the enhanced bone marrow multi-lineage contribution and HSC engraftment persisted (Fig. 5d). A separate cohort of animals competitively transplanted with WBM also showed similar signs of rejuvenation only in the ADRβ3 agonist-treated group, characterized by a reduction in the competitive advantage of old WBM and HSC expansion, indistinguishable from that of saline-treated young mice (Supplementary Fig. 12a–b). We also administered the ADRβ3 agonist BRL37344 to denervated mice and found that it could rescue the premature aging phenotypes (Supplementary Fig. 13a–f), suggesting specificity in the effect of ADRβ3 signaling in the bone marrow microenvironment.

To confirm further that ADRβ3 agonist treatment rejuvenated old HSCs and to obtain further molecular insight, we analyzed the transcriptomes by RNA-seq of HSCs sorted from either young (yHSCs), old (oHSCs) or ADRβ3-agonist rejuvenated old mice (rHSCs). Using t-distributed stochastic neighbor embedding analysis (t-SNE)[55], we found that the rHSC cluster did not overlap with oHSCs and moved closer to yHSCs (Supplementary Fig. 14a), suggesting that ADRβ3 agonist treatment altered the gene expression patterns of old HSCs. Unsupervised hierarchical clustering of top differentially expressed genes also revealed that rHSCs expression signature became similar to yHSCs (Supplementary Fig. 14b). Pathway analysis of top differentially expressed genes between rHSCs and oHSCs revealed downregulation of genes associated with active cell cycle progression, primarily mitosis and cytokinesis (Supplementary Fig. 14c, left), suggesting that treatment with the ADRβ3 agonist impacted cell cycle status of old HSCs, reported to be highly variable and a major contributor of heterogeneity within the aged HSC pool[10,56]. Moreover, upregulation of genes associated with chemokine activity and cytoskeleton organization was detected in rHSCs (Supplementary Fig. 14c, right), pathways reported to be diminished in old HSCs, and contributing to enhanced mobilization and poor homing activity[57–59]. Further evaluation of lineage-selective gene sets, focusing on those reported to be differentially expressed in old HSCs[11], revealed a restoration toward levels in yHSCs, with more profound effects observed for the lymphoid-lineage genes (Fig. 5e). These data indicate that ADRβ3 reprograms an array of pathways that confer rejuvenated phenotypic characteristics.

The rejuvenation of old HSCs was likely mediated by the niche because, in contrast to *Adrb2* which is expressed by HSC and progenitors, neither young nor old HSCs expressed *Adrb3* transcript or responded to ADRβ3 agonist BRL37344 *in vitro* (Supplementary Fig. 10a–b). In keeping with an action of the ADRβ3 agonist on the niche, immunofluorescence imaging of vascular structures and their associated stromal cells revealed partial restoration of arteriolar segment length and α-SMA+ cell density by ADRβ3 agonist treatment

(Supplementary Fig. 14d–f). In addition, a more detailed analysis of CD45$^-$ Ter119$^-$ CD31$^-$ CD51$^+$ PDGFRα$^+$ MSC functional properties revealed significant improvements in *Cxcl12*, *Scf* niche factors and *Ngf* expression (Fig. 5f) and CFU-F activity (Fig. 5g), suggesting a rejuvenated state of aged MSCs. These results suggest that niche rejuvenation by supplementation of ADRβ3 signals in old mice, significantly rejuvenates old HSCs and restored their functional properties.

Deletion of ADRβ3 in mice induces an accelerated aging of HSC niches

Since ADRβ3 mimetics significantly rejuvenated the HSC niche in old mice, we tested whether the constitutive deletion of *Adrb3* (*Adrb3$^{-/-}$*) could lead to premature aging. Serial analyses of *Adrb3$^{-/-}$* and control mice at 2.5 and 5 months of age showed a significant expansion of MSCs with reduced CFU-F and HSC maintenance activities already at 2.5 months (Fig. 5h–j), without detectable alterations in bone marrow cellularity or CD31^{high} total ECs (Supplementary Fig. 15a–b). In addition, while other aging phenotypes such as reduction in Sca-1^{high} CD31^{high} arteriolar ECs (Supplementary Fig. 15c) and HSC expansion (Fig. 5k) were not present at 2.5 months of age, they were apparent at 5 months, suggesting that loss of ADRβ3 signaling in stromal cells may be an initial event leading to premature HSC aging. It is notable that the expanded HSCs were significantly enriched in CD41$^+$ myeloid-biased HSCs[48] (Supplementary Fig. 15d), with reductions in lymphoid-primed multipotent progenitors (LMPPs; Fig. 5l), common lymphoid progenitors (CLPs; Supplementary Fig. 15e), and a trend toward increased common myeloid progenitors (CMPs) and granulocyte-macrophage progenitors (GMPs) (Supplementary Fig. 15f–g), leading to myeloid bias and lymphopenia in peripheral blood (Fig. 5m–n), reminiscent of premature aging. To confirm further that the accelerated aging phenotype observed in *Adrb3$^{-/-}$* mice, derives from the deletion of *Adrb3* in the niche, we carried out reciprocal bone marrow transplantation of young wild-type bone marrow into lethally irradiated control (*Adrb3$^{+/+}$*) or *Adrb3$^{-/-}$* young mice (Supplementary Fig. 15h). To detect premature aging phenotypes, chimeric mice were analyzed at 5 months of age (3 months post transplantation; Supplementary Fig. 15i). We found that *Adrb3* deletion in the microenvironment was sufficient to induce aging-like changes in bone marrow progenitors although the numbers of HSCs and LMPPs were not altered at this time (Supplementary Fig. 15k). Moreover, we detected significant MSC expansion and evidence of myeloid expansion with lymphopenia in the *Adrb3*-deficient niche (Supplementary Fig. 15l–n). Thus, the loss of niche-derived ADRβ3 signaling in young mice promotes premature HSC aging.

Discussion

Here, we show that aging induces significant remodeling of the bone marrow vasculature and its associated stromal cells with progressive loss of SNS innervation. The SNS neuropathy of aging is not a consequence of vascular attrition, but rather an early driver of niche aging, as nerve loss in a model of surgical denervation or genetic deletion of *Adrb3*, can induce dramatic remodeling of the HSC niche. Our results show that the denervation-associated niche remodeling leads to premature aging-like changes in HSCs. The reprogramming of HSCs residing in denervated niches presents all the hallmarks of aging such as poor bone marrow repopulating activity, myeloid bias, and the acquisition of polarity

defects with increased frequency of γH2AX foci[10,12]. Remarkably, we show that the administration of an ADRβ3 agonist can reverse, at least in part, the molecular and functional aging signatures.

Extrinsic factors within the HSC niche have been suggested to contribute to HSC aging. A recent study has found that aging-associated alterations of arterioles was dependent on Notch signaling and that although overexpression of Notch could rescue the vascular phenotype, it could not rejuvenate aged HSCs[18], indicating that HSC aging may depend on a more complex interplay among niche components. Niche-derived soluble factors, including the pro-inflammatory CC-chemokine ligand 5 (CCL5), Osteopontin and CXCL12 have been reported to influence HSC aging[19,21,22]. Our results show that the prolonged loss of ADRβ3 signaling derived from SNS nerves leads to a remodeling of HSC niches that promotes premature aging.

While several intrinsic mechanisms have been proposed to rejuvenate old HSCs[4], the present results highlight key functions of the niche in both aging and rejuvenation of HSC functions. An extrinsic mechanism for BRL37344-mediated rejuvenation is supported by the absence of *Adrb3* expression in HSCs, the lack of direct HSC response to BRL37344, and by the reciprocal transplantation of wild-type bone marrow into *Adrb3*^{−/−} animals, showing that the deficit in ADRβ3 signaling in the microenvironment mediated the premature HSC aging. Given the broad expression changes in rejuvenated HSCs, it is likely that the molecular mechanism(s) of ADRβ3 agonist is(are) complex and may involve multiple pathways emerging from the rejuvenated microenvironment that remain to be defined. In this context, it is interesting that sympathetic neural dysfunction has been described in primary and secondary lymphoid organs, where remodeling of sympathetic innervation in the spleen and thymus caused age-related alterations in the local microenvironment and immune dysfunctions[60]. Our results indicate that local bone marrow neural degeneration may serve as a key driver of aging and provide the proof-of-principle that rejuvenation of old HSCs can be achieved by modulating the neural input to the niche. Protection of endogenous SNS nerves or supplementation of ADRβ3 signals in old age may thus provide an exciting new avenue for niche-targeted stem cell rejuvenation therapy.

Online Methods

Mice

Nestin–GFP mice[25] were bred and aged in our facilities. Aged C57BL/6 mice were obtained from the National Institute of Aging (NIA), or retired breeders obtained from Jackson Laboratory, or by aging young mice (C57BL/6J; Jackson Laboratory) in our facilities for 8, 12 and 24 months. *Adrb3*^{−/−} mice were from the Jackson Laboratory (FVB/N-*Adrb3*[tm1Lowl]/J; stock: 006402) and backcrossed to C57BL/6J background in our facilities. JaB6-Ly5.1 (CD45.1) mice were purchased from the National Cancer Institute or the Jackson laboratory (B6.SJL-*Ptprc*[a] *Pepc*[b]/BoyJ). Unless indicated otherwise, 8 to 10-week-old male and female mice were used as young controls and 20 to 24-month-old males and females were used as old mice. For all analytical and therapeutic experiments, sex-matched animals from the same age group were randomly assigned to experimental groups. This study complied with all ethical regulations involving experiments with mice and the Animal

Care and Use Committee of Albert Einstein College of Medicine approved all experimental procedures.

Competitive HSC and bone marrow transplantation

Competitive repopulation assays were performed using the CD45.1/CD45.2 congenic system. CD45.1 recipient mice were lethally irradiated (12 Gy, two split doses) in a Cesium Mark 1 irradiator (JL Shepherd & Associates). For competitive repopulation assays 1×10^6 CD45.2 donor-nucleated bone marrow cells (BMNCs) were transplanted into irradiated recipients together with 1×10^6 of CD45.1 BMNCs (equal numbers of cells are pooled from donor mice). For competitive HSC repopulation assays, 200 donor HSCs (CD45.2) were sorted from pooled donor bone marrow cells and transplanted into irradiated CD45.1 recipients together with corresponding number of CD45.1 competitor BMNCs calculated to contain 200 HSCs (1:1 HSC ratio). For secondary bone marrow transplantation, 3×10^6 BMNCs from primary recipient chimeric mice were transplanted into lethally irradiated CD45.1 young recipient mice. CD45.1/CD45.2 chimerism of recipient blood and bone marrow was analyzed up to 5 months after transplantation using FACS analysis.

Reciprocal Bone marrow transplantation

For reciprocal bone marrow transplantation, 4×10^6 BMNCs from 2-month-old CD45.1 donor mice were transplanted into lethally irradiated (12 Gy, two split doses) in a Cesium Mark 1 irradiator (JL Shepherd & Associates), $Adrb3^{+/+}$ and $Adrb3^{-/-}$ CD45.2 2 month old recipient mice. CD45.1/CD45.2 donor chimerism of recipient blood and bone marrow was analyzed 3 months after transplantation (5 months old) and mice were analyzed accordingly using FACS analysis.

Sample preparation for flow cytometry and cell sorting

Nucleated single-cell suspensions enriched from bone marrow were obtained by flushing and dissociating BM plugs using a 21G needle in phosphate-buffered saline (PBS; Gibco). Single-cell suspensions enriched from peripheral blood were obtained by retro orbital or cheek bleeding of mice. For analysis of stromal and endothelial cell populations, intact flushed bone marrow plugs were digested for 30 min at 37°C in 1 mg ml^{-1} Collagenase type IV (Gibco) and 2 mg ml^{-1} Dispase (Gibco) in Hank's balanced salt solution (HBSS; Gibco). Compact bones (after flushing out marrow) were crushed and digested in 3 mg ml^{-1} Collagenase type 1A (Sigma) in 1% FBS/HSBSS for 90 min rotating at 37°C. For FACS analysis or sorting, cells were stained with antibodies in PEB (PBS containing 0.5% BSA and 2 mM EDTA). Dead cells and debris were excluded by FSC, SSC and DAPI (4′, 6-diamino-2-phenylindole; Sigma) staining profiles. To eliminate the non-endothelial CD31$^+$ fraction, total ECs quantified by FACS were identified as CD45$^-$ Ter119$^-$ CD31^{high} Sca-1$^+$ and arteriolar ECs were identified as CD45$^-$ Ter119$^-$ CD31^{high} Sca-1^{high}. For sorting ECs, anti-CD31-Alexa Fluor 647 (MEC13.3; 102516) was injected intravenously 10 min prior to sacrificing mice. FACS analyses were carried out using BD LSRII flow cytometer (BD Biosciences) and cell sorting experiments were performed using either BD FACSAria II Cell Sorter (BD Biosciences) or MoFlo Astrios (Beckman Coulter). Data were analyzed with FlowJo 10.0.8 (LLC) or FACS Diva 6.1 software (BD Biosciences).

Flow cytometry antibodies

The following antibodies were used for flow cytometry: anti-Ly6A/E-Alexa Fluor 700 (D7; 56-5981-82), anti-CD117-PE/Cy7 (2B8; 105814), anti-CD45.2-PE (104; 109807), CD45-Pacific Blue (30-F11; 103126), anti-CD31-Alexa Fluor 647 (MEC13.3; 102516), anti-VE-cadherin (CD144)-APC-Alexa Fluor 647 (BV13; 138006), Anti-CD150-PE (TC15-12F12.2; 115904), anti-Ter119-Pacific Blue (TER-119; 116232), anti-CD16/32 (FcγR III/II)-APC/Cy7 (93; 101328) were purchased from BioLegend (San Diego, CA). Anti-CD48-PerCp-eFluor710 (HM48-1; 46-0481-182), anti-CD45.1-FITC (A20; 11-0453-85), anti-CD4-PE/Cy7 (GK1.5; 25-0041-82), anti-CD8a-PE/Cy7 (53-6.7; 25-0081-85), anti-B220-APC-eFluor 780 (RA3-6B2; 47-0452-82), anti-CD11b (Mac-1)-APC-eFluor 780 (M1/70; 47-0112-82), anti-Gr-1 (Ly-6G)- APC-eFluor 780 (RB6-8C5; 47-5931-82), anti-CD3e-APC-eFluor 780 (145-2C11; 47-0031-82), anti-CD45-APC-eFluor 780 (30-F11; 47-0451-82), anti-CD31-PE/Cy7 (MEC13.3; 25-0311-82), anti-PDGFRα (CD140a)-APC (APA5; 17-1401-81), anti-PDGFRα (CD140a)-PE/Cy7 (APA5; 25-1401-82), CD51-PE (RMV-7; 13-0512-85), anti-CD41-FITC (MWReg30; 11-0411-81), anti-Ki-67-PerCp-eFluor 710 (SolA15; 46-5698-80), anti-Ter119-APC-eFluor 780 (TER-119; 47-5921-82), Streptavidin APC-eFluor 780 (47-4317-82), anti-CD34-eFluor 660 (RAM34; 50-0341-82 at 1:50 dilution), anti-CD127 (IL7R)-PerCp (A7R34; 45-1271-80), CD135 (Flt3)-PE (A2F10; 12-1351-83) were purchased from eBioscience (Thermo Fisher). Anti-lineage panel cocktail (TER-119, RB6-8C5, RA3-6B2, M1/70, 145-2C11 at 1:50 dilution) was from BD Biosciences (559971). Unless otherwise specified, all antibodies were used at a 1:100 dilution. All antibodies were anti-mouse and their specificity was validated in previous studies performed in our laboratory[25,28,36,43,54,61].

In vitro culture assays

Hematopoietic progenitor colony-forming units in culture (CFU-C) assay was done as previously described[61]. HSC culture was done as previously described[28], in the presence or absence of either 10, 25, 50 or 100 μM BRL37344 (Sigma). MSC culture, CFU-F and mesensphere formation assay were done by plating freshly sorted CD45− Ter119− CD31− CD51+ PDGFRα+ MSCs from digested bone marrow or CD45− Ter119− CD31− Nestin-GFP+ MSCs from digested compact bone and plated at clonal densities in 6 well plates (CFU-F: 1000 cells/well and mesenspheres: 3000 cells/well) under culture conditions previously described[43]. Cells were cultured for 12–14 days upon which the colonies and spheres were scored. For CFU-C and mesensphere cultures low adhesion tissue culture plates (Stem Cell Technologies) were used.

Cell cycle analysis

Analyses of the cell cycle were performed as described previously[25]. Briefly, single cell suspension was stained for cell surface markers and subsequently fixed with Cytofix/Cytoperm fixation and permeabilization solution (BD Biosciences), according to manufacturer's instructions. The cells were then stained with anti-Ki67 antibody (eBioscience) and Hoechst 33342 (Sigma) at 20 μg ml^{-1} for 30 min.

Bone marrow denervation by transaction of femoral and sciatic nerves

Denervation of the femoral and tibial bone marrow was done as previously described[46,47]. The femoral nerve was localized after its exit from the vertebral column deep in the psoas muscle. This was accomplished with a midline abdominal incision, and gently moving the intestines aside to visualize the psoas muscle. An incision was made in the psoas to visualize the femoral nerve, and a 1 cm section of the nerve was excised. Deep to the psoas (through the incision) the sciatic nerve was visualized in close proximity to the iliac crest of the pelvis, and a 1 cm section of the nerve was excised. For sham operation, both femoral and sciatic nerves were exposed by surgery, but were left intact.

Musculo-cutaneous sensory and motor denervation

As previously descried[51], to denervate the hindlimb to induce immobilization without affecting bone marrow innervation, 1 cm of the sciatic nerve was transacted distal to the spinal cord and close to the sciatic notch and 1 cm of the femoral nerve was transacted distal to the spinal cord after exiting the abdomen inferior to the inguinal ligament. For sham operation, same sites of both femoral and sciatic nerves were exposed by surgery, but left intact.

Immunofluorescence staining and imaging of whole-mount sternal tissues and frozen sections of long bones

Whole-mount tissue preparation, immunofluorescence staining and imaging of the sternum was performed as described previously[25,54]. Antibodies used for HSC stains are: Anti-lineage panel cocktail (TER-119, RB6-8C5, RA3-6B2, M1/70, 145-2C11 at 1:50 dilution) from BD Biosciences (559971), anti-CD48-biotin (HM48-1; 13-0481-80, 1:100 dilution), CD41-biotin (MWReg30; 11-0411-82, 1:2500 dilution) from eBioscience (Thermo Fisher) and anti-CD31-Alexa Fluor 647 (MEC13.3; 102516), anti-CD144 (VE-cadherin)-APC-Alexa Fluor 647 (BV13; 138006), Anti-CD150-PE (TC15-12F12.2; 115904 at 1:100 dilution) from Biolegend (San Diego, CA). For all imaging experiments, anti-CD31 and anti-CD144 antibodies were injected intravenously to mice (10 μg, 20 μl of 0.5 μg μl^{-1}) and mice were sacrificed 10 minutes after injection. For frozen sections of long bones, femurs and tibias were fixed in 4% Paraformaldehyde (PFA) overnight at 4°C. For cryopreservation, the bones were incubated sequentially in 10%, 20% and 30% Sucrose/PBS at 4°C, 1 h each, and embedded and flash frozen in SCEM embedding medium (SECTION-LAB). Frozen sections were prepared 20 μm thick with a Cryostat (CM3050, Leica) using the Kawamoto's tape transfer method[62]. For immunofluorescence staining, sections were rinsed with PBS, post-fixed with 4% cold PFA for 10 min followed by blocking with 20% Donkey Serum (DS; Sigma) in 0.5% Triton X-100/PBS for 3 h at room temperature. For SNS nerve staining, anti-Tyrosine Hydroxylase (TH) antibody (Cat: AB152; Lot: 2493925; Millipore) was used at 1:100 dilution in 2% DS 0.1% Triton X-100/PBS for 72 h at 4°C. For pan-neural staining, Alexa Fluor 488 conjugated anti-Tubulin Beta3 (Tubb3) antibody (Clone: AA10; Cat: 657404; Biolegend) was used at 1:100 dilution in 2% DS 0.1% Triton X-100/PBS for 72 h at 4°C. For Synaptophysin staining, rabbit polyclonal anti-Synaptophysin (Cat: ab32594; Abcam) antibody was used at 1:100 dilution in 2% DS 0.1% Triton X-100/PBS for 72 h at 4°C. For Perilipin staining, rabbit polyclonal anti-Perilipin antibody (Clone: D1D8;

Cat: 9349; Cell Signaling Technology) was used at 1:100 dilution in 2% DS 0.1% Triton X-100/PBS overnight at 4°C. For α-SMA staining, monoclonal anti-Actin α-Smooth Muscle - Cy3-conjugated antibody (Clone: 1A4; Cat: C6198; Sigma) was used at 1:100 dilution in 2% DS 0.1% Triton X-100/PBS for 30 min at room temperature. When necessary, primary antibody staining was followed by 3 washes with 2% DS 0.1% Triton X-100/PBS and 30 min incubation with Alexa Fluor 568-conjugated goat anti-rabbit IgG (Cat: A11011, Invitrogen) secondary antibody and 0.2% DAPI (4′, 6-diamino-2-phenylindole; Sigma. All images were acquired at room temperature using ZEISS AXIO examiner D1 microscope (Zeiss) with confocal scanner unit (Yokogawa), and reconstructed in three dimensions with Slide Book software (Intelligent Imaging Innovations). Image analysis was performed using both Slide Book software (Intelligent Imaging Innovations) and Fiji build of ImageJ (NIH).

Immunofluorescence staining and imaging of sorted HSCs

Immunofluorescence staining for either γH2AX or Cdc42 and Tubulin was adapted from[10,17]. Lineage− CD48− Sca-1+ c-Kit+ CD150+ HSCs were directly sorted on poly-lysine coated slides (P0425-72AE; Sigma), 500–2000 cells per slide, incubated for 10 min, fixed with 4% PFA for 10 min at room temperature, and permeabilized with 0.2% Triton X-100 for 20 min at room temperature. Consequently, the cells were blocked with 1% BSA/PBS overnight at 4°C. For γH2AX staining, cells were incubated with 0.125 μg (5 μl of 25 μg ml^{-1}) FITC-conjugated anti-phospho H2A.X (ser139) antibody (Clone: 2F3; Cat: 613404; Biolegend) for 2 h at 37°C. Primary antibody staining was followed by 3 washes with PBS and 10 min incubation with 0.2% DAPI (Sigma). For Cdc42 and Tubulin staining, cells were incubated with rabbit polyclonal anti-Cdc42 antibody (1:50 dilution, Cat: 07-1466; Millipore) and rat monoclonal anti-Tubulin antibody (1:100 dilution, Clone: YL1/2; Cat: ab6160; Abcam) for 2 h at 37°C. Primary antibody staining was followed by 3 washes with PBS and 1 h incubation at room temperature with Alexa Fluor 633-conjugated goat anti-rabbit IgG (Cat: A21071; Invitrogen) and Alexa Fluor 488-conjugated goat anti-rat IgG (Cat: A11006; Invitrogen) both at 1:100 dilution. Secondary antibody staining was followed by 3 washes with PBS and 10 min incubation with 0.2% DAPI (Sigma). All images were acquired using ZEISS AXIO examiner D1 microscope (Zeiss) with confocal scanner unit (Yokogawa), and reconstructed in three dimensions with Slide Book software (Intelligent Imaging Innovations). Image analysis was performed using the Slide Book software (Intelligent Imaging Innovations).

RNA isolation and quantitative real time PCR (Q-PCR)

RNA isolation and Q-PCR was performed as described previously[25]. All mRNA expression levels were calculated relative to *Gapdh* or *Actb*. To ascertain that the expression levels of the housekeeping genes did not change with age, for all experiments, *Actb* mRNA levels were quantified relative to *Gapdh* and did not show any changes. The sequences of the oligonucleotides used can be provided upon request.

RNA-seq and analysis

Total RNA from 2000 sorted HSCs was extracted using the RNAeasy Plus Micro kit (Qiagen), and assessed for integrity and purity using an Aligent 2100 Bioanalyzer (Agilent

Technologies). Complementary DNA libraries were then generated using the SMART-Seq v4 Ultra Low Input RNA Kit for Sequencing (Clontech Laboratories) and the Nextera XT DNA Sample preparation Kit (Illumina). The libraries were then submitted for Illumina NextSeq 500 sequencing (150bp single ended) according to the standard procedures. (ENSEMBL Mus musculus reference genome GRCm38 release 77). RNA-Seq data generated from Illumina NextSeq 500 were processed using the following pipeline. Briefly, single- and double-ended sequencing reads were aligned to the mouse genome (mm10) using Spliced Transcripts Alignment to a Reference (STAR 2.5.3a). Aligned reads were then quantified to transcriptome (mm10 - Ensembl Transcripts release 83), normalized and differentially expressed genes were identified using Partek Flow. Hierarchical clustering and Gene Set Enrichment Analysis (GSEA) were then performed on the top 150 variable genes. (For citing the GSEA software, please reference Subramanian, Tamayo, et al.[63] and Mootha, Lindgren, et al.[64]

In vivo administration of β-adrenergic agonists

For long-term administration of β-adrenergic agonists, Clenbuterol (Sigma) and BRL37344 (Sigma) were dosed at 2 mg Kg^{-1} day^{-1} and 2.4 mg Kg^{-1} day^{-1}, respectively, using subcutaneously implanted Alzet osmotic pumps (model 2006; DURECT Corporation). Six weeks following implantation of the first pump, an additional pump was implanted for a total of 12 weeks of continuous drug delivery. Control animals were implanted with Alzet pumps containing saline (PBS; Gibco).

Statistics and reproducibility

All data are represented as mean ± s.e.m. No statistical method was used to predetermine sample size. Sample size was determined by previous experience with similar models of hematopoiesis as shown in previous experiments done in our laboratory[24,25,28,36,43,54]. For all experiments, mice were randomly assigned to experimental groups and no sample blinding was utilized for experiment collection or analysis. Sample exclusion was only done as a result of premature mouse death or infection due injury or improper healing post-surgery. Experiments presented were successfully reproduced at least 3 times. For box plots, box span from the 25th to 75th percentiles and the centerline is plotted at the median. Whiskers represent minimum to maximum range. Comparisons between two groups were done using the unpaired two-tailed *t* test and paired two-tailed *t* test for denervation experiments. The t ratio was calculated as difference between sample means divided by the standard error of the difference and calculated by combining the s.e.m. of the two groups. Degrees of freedom (df) were calculated as total sample size - 2 (t-values and degrees of freedom are provided in source data). One-way ANOVA Tukey's multiple comparisons test was used for multiple group comparisons, Two-way ANOVA Bonferroni's multiple comparison tests was used for multiple parameter analysis and Two-sample Kolmogorov–Smirnov tests was used for comparisons of distribution patterns. Data statistical analyses analyses and presentation were performed using either GraphPad Prism 7 (GraphPad Software, San Diego, CA), FACS Diva 6.1 software (BD Biosciences), FlowJo 10.0.8 (LLC), Slide Book software (Intelligent Imaging Innovations) and Fiji build of ImageJ (NIH).

Life Sciences Reporting Summary

Further information on experimental design is available in the Life Sciences Reporting Summary.

Data Availability

RNA sequencing data has been deposited in the Gene Expression Omnibus under accession number GSE109546. Source data for all 5 main figures is available online. All other source data is available upon reasonable request from the corresponding author.

Supplementary Material

Refer to Web version on PubMed Central for supplementary material.

References

1. López-Otín C, Blasco MA, Partridge L, Serrano M, Kroemer G. The Hallmarks of Aging. Cell. 2013; 153:1194–1217. [PubMed: 23746838]

2. Signer Robert AJ, Morrison Sean J. Mechanisms that Regulate Stem Cell Aging and Life Span. Cell Stem Cell. 2013; 12:152–165. [PubMed: 23395443]

3. Orkin SH, Zon LI. Hematopoiesis: An Evolving Paradigm for Stem Cell Biology. Cell. 2008; 132:631–644. [PubMed: 18295580]

4. Guidi N, Geiger H. Rejuvenation of aged hematopoietic stem cells. Seminars in Hematology. 2017; 54:51–55. [PubMed: 28088989]

5. Ho TT, et al. Autophagy maintains the metabolism and function of young and old stem cells. Nature. 2017; 543:205. [PubMed: 28241143]

6. Chen C, Liu Y, Liu Y, Zheng P. mTOR Regulation and Therapeutic Rejuvenation of Aging Hematopoietic Stem Cells. Science Signaling. 2009; 2:ra75. [PubMed: 19934433]

7. Mohrin M, et al. A mitochondrial UPR-mediated metabolic checkpoint regulates hematopoietic stem cell aging. Science. 2015; 347:1374. [PubMed: 25792330]

8. Norddahl Gudmundur L, , et al. Accumulating Mitochondrial DNA Mutations Drive Premature Hematopoietic Aging Phenotypes Distinct from Physiological Stem Cell Aging. Cell Stem Cell. 2011; 8:499–510. [PubMed: 21549326]

9. Warr MR, et al. FOXO3A directs a protective autophagy program in haematopoietic stem cells. Nature. 2013; 494:323. [PubMed: 23389440]

10. Flach J, et al. Replication stress is a potent driver of functional decline in ageing haematopoietic stem cells. Nature. 2014; 512:198–202. [PubMed: 25079315]

11. Rossi DJ, et al. Cell intrinsic alterations underlie hematopoietic stem cell aging. Proceedings of the National Academy of Sciences of the United States of America. 2005; 102:9194–9199. [PubMed: 15967997]

12. Rossi DJ, et al. Deficiencies in DNA damage repair limit the function of haematopoietic stem cells with age. Nature. 2007; 447:725–729. [PubMed: 17554309]

13. Beerman I, Seita J, Inlay Matthew A, Weissman Irving L, Rossi Derrick J. Quiescent Hematopoietic Stem Cells Accumulate DNA Damage during Aging that Is Repaired upon Entry into Cell Cycle. Cell Stem Cell. 2014; 15:37–50. [PubMed: 24813857]

14. Moehrle Bettina M, , et al. Stem Cell-Specific Mechanisms Ensure Genomic Fidelity within HSCs and upon Aging of HSCs. Cell Reports. 2015; 13:2412–2424. [PubMed: 26686632]

15. Guidi N, Geiger H. Rejuvenation of aged hematopoietic stem cells. Seminars in Hematology. 54:51–55. [PubMed: 28088989]

16. Beerman I, Rossi DJ. Epigenetic regulation of hematopoietic stem cell aging. Experimental cell research. 2014; 329:192–199. [PubMed: 25261778]

17. Florian Maria C, , et al. Cdc42 Activity Regulates Hematopoietic Stem Cell Aging and Rejuvenation. Cell Stem Cell. 2012; 10:520–530. [PubMed: 22560076]

18. Kusumbe AP, et al. Age-dependent modulation of vascular niches for haematopoietic stem cells. Nature. 2016; 532:380–384. [PubMed: 27074508]

19. Guidi N, et al. Osteopontin attenuates aging - associated phenotypes of hematopoietic stem cells. The EMBO Journal. 2017; 36:840. [PubMed: 28254837]

20. Poulos MG, et al. Endothelial transplantation rejuvenates aged hematopoietic stem cell function. The Journal of Clinical Investigation. 2017; 127:4163–4178. [PubMed: 29035282]

21. Ergen AV, Boles NC, Goodell MA. Rantes/Ccl5 influences hematopoietic stem cell subtypes and causes myeloid skewing. Blood. 2012; 119:2500. [PubMed: 22289892]

22. Tuljapurkar SR, et al. Changes in human bone marrow fat content associated with changes in hematopoietic stem cell numbers and cytokine levels with aging. Journal of Anatomy. 2011; 219:574–581. [PubMed: 21923862]

23. Mendelson A, Frenette PS. Hematopoietic stem cell niche maintenance during homeostasis and regeneration. Nat Med. 2014; 20:833–846. [PubMed: 25100529]

24. Mendez-Ferrer S, et al. Mesenchymal and haematopoietic stem cells form a unique bone marrow niche. Nature. 2010; 466:829–834. [PubMed: 20703299]

25. Kunisaki Y, et al. Arteriolar niches maintain haematopoietic stem cell quiescence. Nature. 2013; 502:637–643. [PubMed: 24107994]

26. Ding L, Morrison SJ. Haematopoietic stem cells and early lymphoid progenitors occupy distinct bone marrow niches. Nature. 2013; 495:231–235. [PubMed: 23434755]

27. Itkin T, et al. Distinct bone marrow blood vessels differentially regulate haematopoiesis. Nature. 2016; 532:323–328. [PubMed: 27074509]

28. Bruns I, et al. Megakaryocytes regulate hematopoietic stem cell quiescence through CXCL4 secretion. Nat Med. 2014; 20:1315–1320. [PubMed: 25326802]

29. Kiel MJ, et al. SLAM Family Receptors Distinguish Hematopoietic Stem and Progenitor Cells and Reveal Endothelial Niches for Stem Cells. Cell. 2005; 121:1109–1121. [PubMed: 15989959]

30. Yamazaki S, et al. Nonmyelinating Schwann cells maintain hematopoietic stem cell hibernation in the bone marrow niche. Cell. 2011; 147:1146–1158. [PubMed: 22118468]

31. Katayama Y, et al. Signals from the Sympathetic Nervous System Regulate Hematopoietic Stem Cell Egress from Bone Marrow. Cell. 2006; 124:407–421. [PubMed: 16439213]

32. Mendez-Ferrer S, Lucas D, Battista M, Frenette PS. Haematopoietic stem cell release is regulated by circadian oscillations. Nature. 2008; 452:442–447. [PubMed: 18256599]

33. Maestroni G, et al. Neural and endogenous catecholamines in the bone marrow. Circadian association of norepinephrine with hematopoiesis? Experimental Hematology. 1998; 26:6.

34. Méndez-Ferrer S, Battista M, Frenette PS. Cooperation of β2- and β3-adrenergic receptors in hematopoietic progenitor cell mobilization. Annals of the New York Academy of Sciences. 2010; 1192:139–144. [PubMed: 20392229]

35. Scheiermann C, et al. Adrenergic Nerves Govern Circadian Leukocyte Recruitment to Tissues. Immunity. 2012; 37:290–301. [PubMed: 22863835]

36. Lucas D, et al. Chemotherapy-induced bone marrow nerve injury impairs hematopoietic regeneration. Nat Med. 2013; 19:695–703. [PubMed: 23644514]

37. Zhao M, et al. Megakaryocytes maintain homeostatic quiescence and promote post-injury regeneration of hematopoietic stem cells. Nat Med. 2014; 20:1321–1326. [PubMed: 25326798]

38. Hanoun M, et al. Acute Myelogenous Leukemia-Induced Sympathetic Neuropathy Promotes Malignancy in an Altered Hematopoietic Stem Cell Niche. Cell Stem Cell. 2014; 15:365–375. [PubMed: 25017722]

39. Arranz L, et al. Neuropathy of haematopoietic stem cell niche is essential for myeloproliferative neoplasms. Nature. 2014; 512:78–81. [PubMed: 25043017]

40. Thiel G. Synapsin I, Synapsin II, and Synaptophysin: Marker Proteins of Synaptic Vesicles. Brain Pathology. 1993; 3:87–95. [PubMed: 7903586]

41. Magnon C, et al. Autonomic Nerve Development Contributes to Prostate Cancer Progression. Science. 2013; 341

42. Levi-Montalcini R. The nerve growth factor 35 years later. Science. 1987; 237:1154–1162. [PubMed: 3306916]

43. Pinho S, et al. PDGFRα and CD51 mark human Nestin+ sphere-forming mesenchymal stem cells capable of hematopoietic progenitor cell expansion. The Journal of Experimental Medicine. 2013; 210:1351–1367. [PubMed: 23776077]

44. Ambrosi TH, et al. Adipocyte Accumulation in the Bone Marrow during Obesity and Aging Impairs Stem Cell-Based Hematopoietic and Bone Regeneration. Cell Stem Cell. 2017; 20:771–784.e776. [PubMed: 28330582]

45. Young K, et al. Progressive alterations in multipotent hematopoietic progenitors underlie lymphoid cell loss in aging. The Journal of Experimental Medicine. 2016; 213:2259. [PubMed: 27811054]

46. Afan AM, Broome CS, Nicholls SE, Whetton AD, Miyan JA. Bone marrow innervation regulates cellular retention in the murine haemopoietic system. British Journal of Haematology. 1997; 98:569–577. [PubMed: 9332309]

47. Miyan JA, Broome CS, Whetton AD. Neural Regulation of Bone Marrow. Blood. 1998; 92:2971–2972.

48. Gekas C, Graf T. CD41 expression marks myeloid-biased adult hematopoietic stem cells and increases with age. Blood. 2013; 121:4463. [PubMed: 23564910]

49. Sudo K, Ema H, Morita Y, Nakauchi H. Age-Associated Characteristics of Murine Hematopoietic Stem Cells. The Journal of Experimental Medicine. 2000; 192:1273. [PubMed: 11067876]

50. Morrison SJ, Wandycz AM, Akashi K, Globerson A, Weissman IL. The aging of hematopoietic stem cells. Nature Medicine. 1996; 2:1011.

51. Rinkevich Y, et al. Clonal analysis reveals nerve-dependent and independent roles on mammalian hind limb tissue maintenance and regeneration. Proceedings of the National Academy of Sciences. 2014; 111:9846–9851.

52. Benestad HB, Strøm-Gundersen I, Ole Iversen P, Haug E, Njå A. No Neuronal Regulation of Murine Bone Marrow Function. Blood. 1998; 91:1280–1287. [PubMed: 9454758]

53. Cabezas-Wallscheid N, et al. Identification of Regulatory Networks in HSCs and Their Immediate Progeny via Integrated Proteome, Transcriptome, and DNA Methylome Analysis. Cell Stem Cell. 2014; 15:507–522. [PubMed: 25158935]

54. Asada N, et al. Differential cytokine contributions of perivascular stem cell niches. Nat Cell Biol. 2017

55. van der Maaten L, Hinton G. Visualizing Data using t-SNE. Journal of Machine Learning Research. 2008; 9:2579–2605.

56. Kowalczyk MS, et al. Single-cell RNA-seq reveals changes in cell cycle and differentiation programs upon aging of hematopoietic stem cells. Genome Research. 2015; 25:1860–1872. [PubMed: 26430063]

57. Xing Z, et al. Increased hematopoietic stem cell mobilization in aged mice. Blood. 2006; 108:2190. [PubMed: 16741255]

58. Geiger H, Koehler A, Gunzer M. Stem Cells, Aging, Niche, Adhesion and Cdc42: A Model for Changes in Cell-Cell Interactions and Hematopoietic Stem Cell Aging. Cell Cycle. 2007; 6:884–887. [PubMed: 17404508]

59. Liang Y, Van Zant G, Szilvassy SJ. Effects of aging on the homing and engraftment of murine hematopoietic stem and progenitor cells. Blood. 2005; 106:1479. [PubMed: 15827136]

60. Bellinger DL, , et al. Age-Related Alterations in Autonomic Nervous System Innervation of Lymphoid Tissue. In: Lajtha A, Galoyan A, Besedovsky HO, editorsHandbook of Neurochemistry and Molecular Neurobiology: Neuroimmunology. Springer US; Boston, MA: 2008. 61–81.

61. Pierce H, et al. Cholinergic Signals from the CNS Regulate G-CSF-Mediated HSC Mobilization from Bone Marrow via a Glucocorticoid Signaling Relay. Cell Stem Cell. 2017

62. Kawamoto T, Shimizu M. A method for preparing 2- to 50-micron-thick fresh-frozen sections of large samples and undecalcified hard tissues. Histochem Cell Biol. 2000; 113:8.

63. Subramanian A, et al. Gene set enrichment analysis: A knowledge-based approach for interpreting genome-wide expression profiles. Proceedings of the National Academy of Sciences. 2005; 102:15545–15550.

64. Mootha VK, et al. PGC-1α-responsive genes involved in oxidative phosphorylation are coordinately downregulated in human diabetes. Nature Genetics. 2003; 34:267. [PubMed: 12808457]
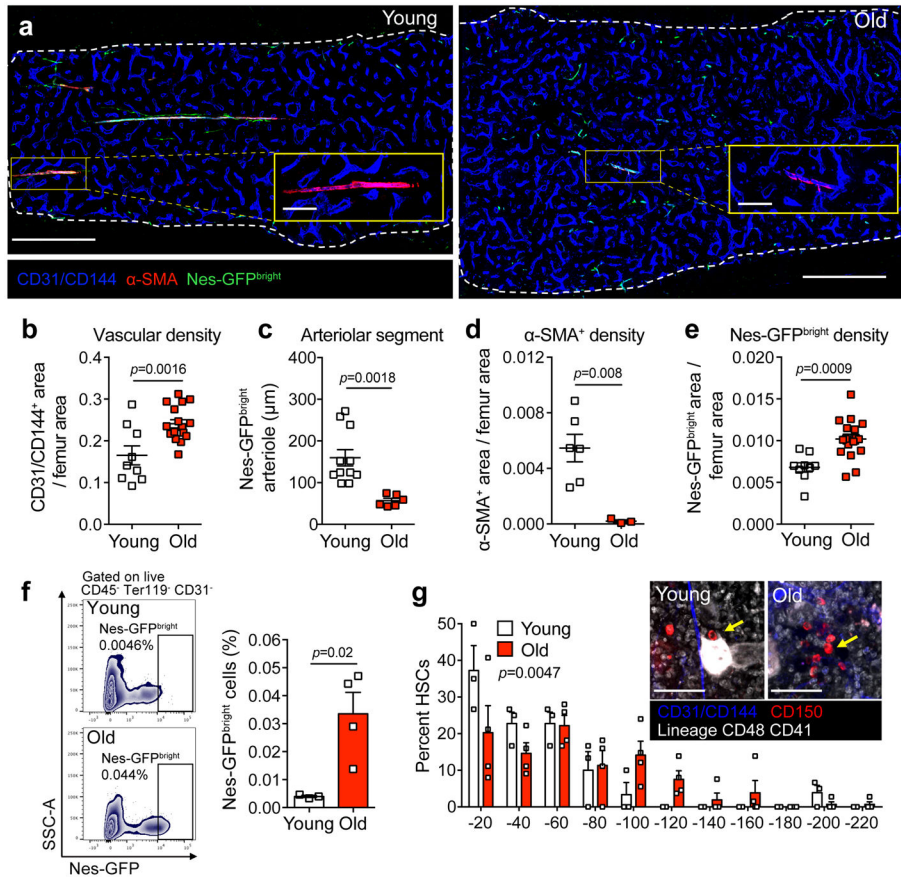
Figure 1. Aging induces remodeling of the HSC niche

(a) Representative confocal z-stack projection montages of femurs from young (2 months) and old (20–24 months) *Nestin-GFP* mice stained for double positive CD31+/CD144+ vasculature and α-SMA+ cells with anti-CD31, anti-CD144 and anti-α-SMA antibodies. Scale bars, 500 μm for montages, 100 μm for zoomed projections, three independent experiments yielded similar results. **(b)** Vascular density in young and old mice, as assessed by quantification of CD31+/CD144+ double positive vascular area divided by total femur area (n=9 and 17 projections in young and old mice, respectively; 4 mice per group). **(c)** Arteriolar segment length in femurs of young and old *Nestin-GFP* mice, as assessed by quantification of the length of the Nestin-GFP^bright signal covering CD31+/CD144+ double positive arterioles (n=11 and 6 projections in young and old mice, respectively; 4 mice per group). **(d)** α-SMA+ cell density in young and old mice, as assessed by quantification of α-SMA+ area divided by total femur area (1 projection per mouse in young (n=6) and old (n=3) mice). **(e)** Nestin-GFP^bright density in young and old mice, as assessed by quantification of Nestin-GFP^bright area divided by total femur area (n=9 and 17 projections in young and old mice, respectively; 4 mice per group) **(f)** Left, representative FACS plots of CD45− Ter119− CD31− Nes-GFP^bright MSCs isolated from young (top) and old (bottom) *Nestin-GFP* mice. Right, the frequency of Nes-GFP^bright MSCs from young and old *Nestin-GFP* mice (n=3 young, 4 old mice). **(g)** Representative whole-mount projections (inset) and quantification of the distribution of lineage− CD41− CD48− CD150+ phenotypic HSCs in the

sternal bone marrow relative to Nestin-GFP^{bright} CD31$^+$/CD144$^+$ double positive arterioles in young and old C57BL/6 mice (n = 47 young HSCs; 148 old HSCs; 3 mice per group). Arrows denote HSCs. Two-sample Kolmogorov-Smirnov test, p = 0.0047. Scale bar, 100 μm. Data represented as mean ± s.e.m, p value determined by two-tailed t-test unless indicated otherwise.
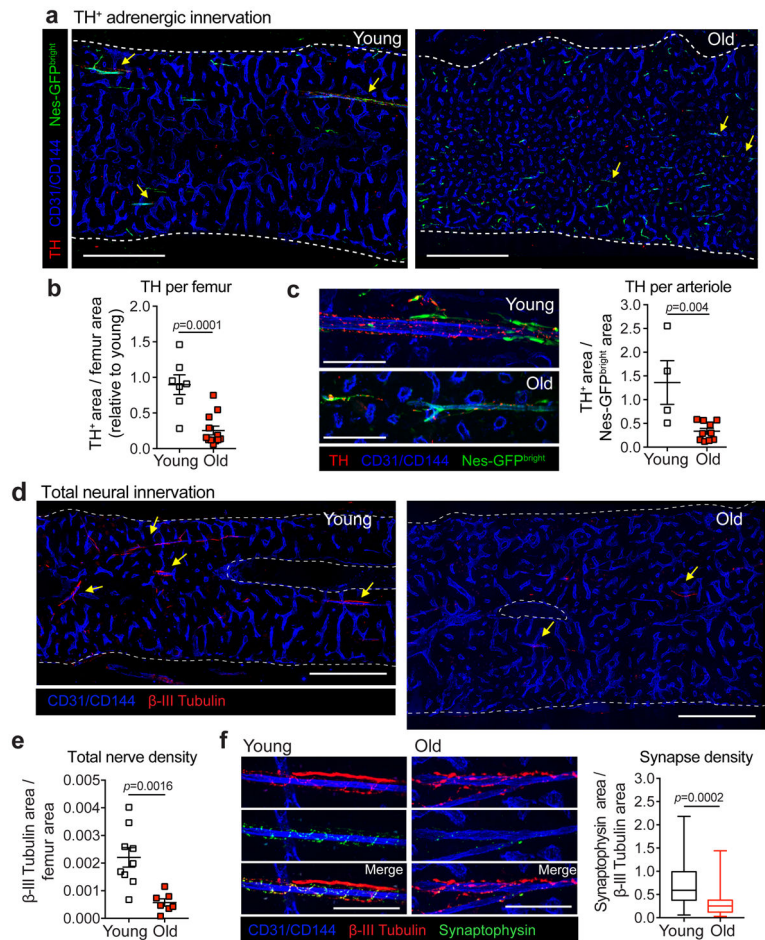
Figure 2. Aging induces the loss of niche-associated adrenergic nerves

(a) Representative confocal *z*-stack projection montages from the bone marrow of young and old *Nestin-GFP* mice stained for CD31$^+$ CD144$^+$ double-positive vasculature and Tyrosine Hydroxylase (TH) positive nerve fibers. Scale bar, 500 μm. Arrows denote TH$^+$ nerves. (b) Femoral adrenergic innervation quantified by TH$^+$ area divided by total femur area (normalized to young; n=7 and 12 old projections in young and old mice, 4 mice per group). (c) Left, representative confocal *z*-stack projections from the bone marrow of young and old *Nestin-GFP* mice stained for CD31$^+$ CD144$^+$ double-positive vasculature and TH$^+$ nerve fibers. Scale bar, 100 μm. Right arteriolar adrenergic innervation quantified by TH$^+$ area divided by total Nestin-GFP^{bright} arteriole area (normalized to young; n=4 and 10 projections in young and old mice, respectively; 4 mice per group). (d) Representative confocal *z*-stack projection montages from the femurs of young and old C57BL/6 mice stained for CD31$^+$ CD144$^+$ double-positive vasculature and β-III Tubulin$^+$ nerve fibers. Scale bar, 500 μm. Arrows denote β-III Tubulin$^+$ nerves. (e) Total femoral innervation quantified by β-III Tubulin$^+$ area divided by total femur area (n=9 and 7 projections in young and old mice, respectively; 3 mice per group). (f) Left, representative confocal *z*-stack projections from femurs of young and old C57BL/6 mice stained for CD31$^+$ CD144$^+$ double-positive vasculature, β-III Tubulin$^+$ nerve fibers and Synaptophysin$^+$ synaptic vesicles. Scale bar, 100 μm. Right, synapse density as assessed by quantification of

Synaptophysin[+] area per β-III Tubulin[+] nerve area (n=54 and 27 projections in young and old mice, respectively; 3 mice per group). Data represented as mean ± s.e.m, p value determined by two-tailed t-test. At least three independent experiments yielded similar results presented in (**a**) and (**d**). For box plots, the box spans from the 25th to 75th percentiles and the centerline is plotted at the median. Whiskers represent minimum to maximum range.
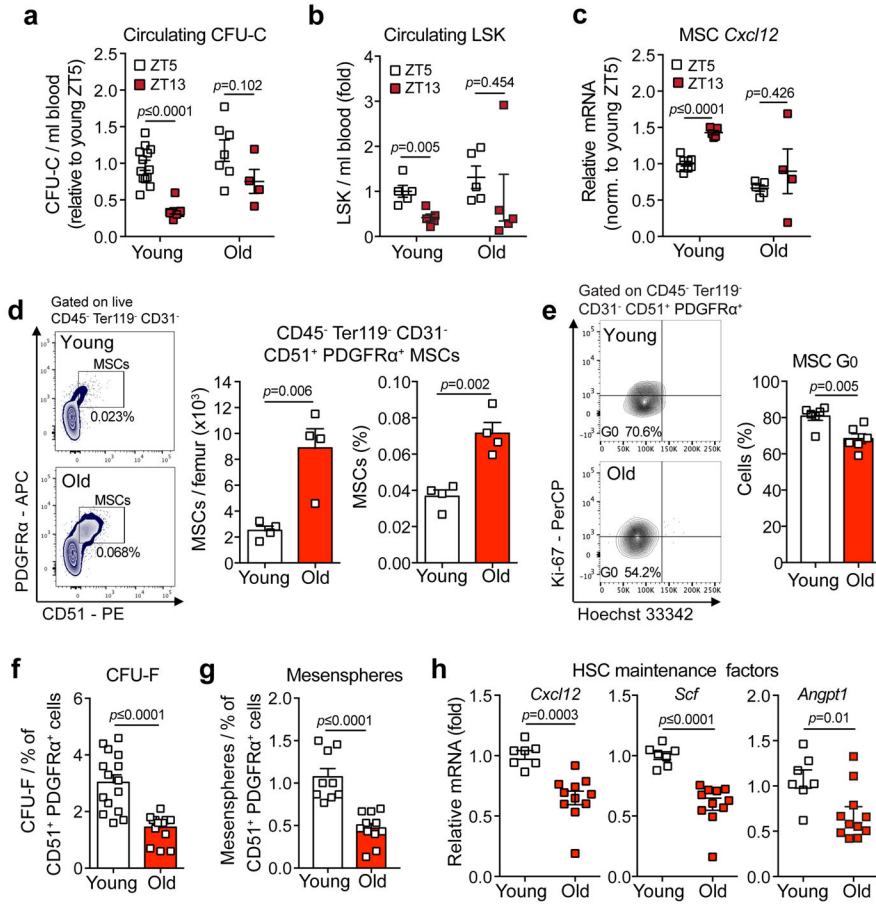
Figure 3. Aging expands MSCs and reduces their HSC maintenance activity
(a, b) Circadian oscillations of circulating CFU-C (normalized to young at ZT5; n=13 young ZT5, 7 old ZT5, 7 young ZT13 and 4 old ZT13 mice) **(a)** and lineage⁻ Sca-1⁺ c-Kit⁺ (LSK) progenitors (normalized to young at ZT5; n=5 mice per group) **(b)** in peripheral blood of young and old C57BL/6 mice. **(c)** Quantification of *Cxcl12* mRNA levels relative to *Actb* in sorted MSCs from young and old C57BL/6 mice at ZT5 and ZT13 (normalized to young at ZT5; n=8 young ZT5, 5 old ZT5, 5 young ZT13 and 4 old ZT13 mice). **(d)** Left, representative FACS plots showing the gating strategy for CD45⁻ Ter119⁻ CD31⁻ CD51⁺ PDGFRα⁺ MSCs in young (top) and old (bottom) C57BL/6 mice. Right, absolute numbers and frequency of MSCs in young and old C57BL/6 mice (n=4 mice per group). **(e)** Left, representative FACS plots showing the gating strategy for MSCs Ki-67 and Hoechst 33342 staining in young (top) and old (bottom) C57BL/6 mice. Right, quantification of Ki-67⁻ G0 MSCs in young and old C57BL/6 mice (n=6 mice per group). **(f, g)** Frequency of CFU-F (n=15 cultures per group) **(f)** and mesenspheres (n=9 young, 11 old cultures) **(g)** from sorted MSCs plated at equal numbers and clonal densities under CFU-F or mesensphere culture conditions (n=5 mice per group). **(h)** Quantification of mRNA levels of *Cxcl12, Scf* and *Angpt1* relative to *Gapdh* in sorted MSCs (normalized to young; n=7 young, 11 old mice). Data represented as mean ± s.e.m, *p* value determined by two-tailed *t*-test.
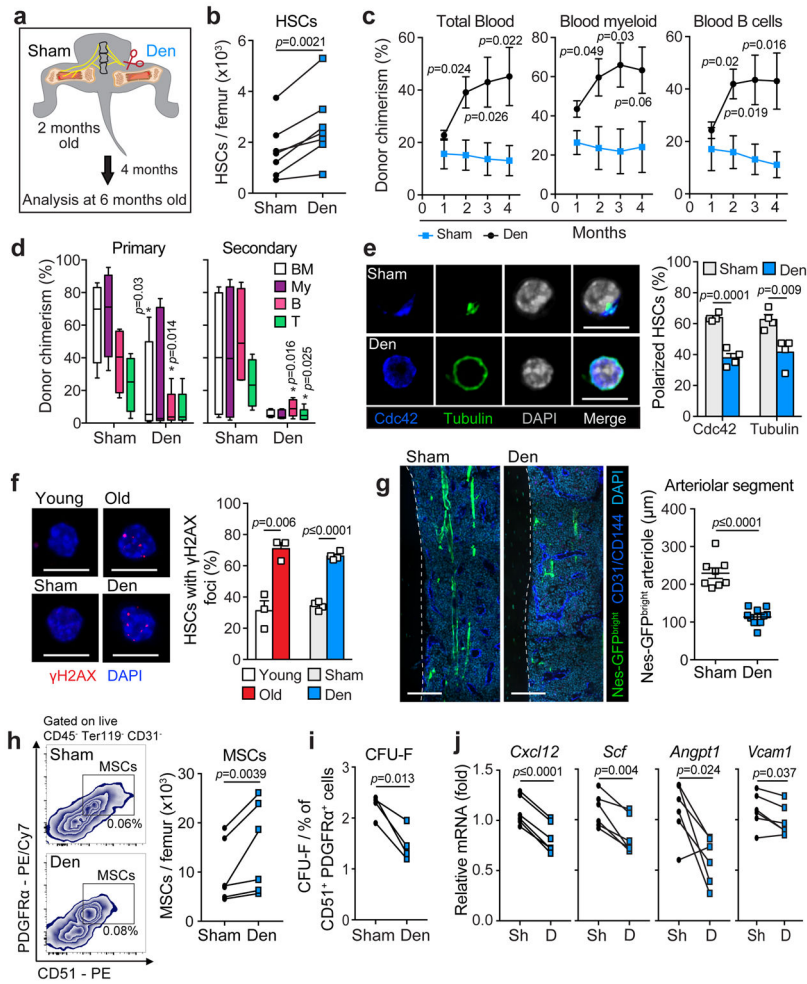
Figure 4. Surgical denervation of young bone marrow induces premature HSC and niche aging
(a) Schematic illustration of surgical denervation experiment. The sciatic and femoral nerves were transected in young (2 months old) C57BL/6 mice and the mice were analyzed 4 months post surgery, at 6 months of age. **(b)** Absolute numbers of HSCs (lineage$^-$ Sca-1$^+$ c-Kit$^+$ CD48$^-$ CD150$^+$) isolated from Sham and Denervated (Den) femurs (n=7 mice). **(c, d)** Total peripheral blood (CD45.2$^+$), blood myeloid (Mac-1$^+$ CD45.2$^+$) and blood B cell (B220$^+$ CD45.2$^+$) donor chimerism at the indicated time points post transplantation **(c)** and bone marrow donor chimerism (Total CD45.2$^+$ (BM); Myeloid (My), Mac-1$^+$ CD45.2$^+$; B cell (B), B220$^+$ CD45.2$^{+;}$ and T cell (T), CD4$^+$/CD8$^+$ CD45.2$^+$) 5 months after primary transplantation of 200 HSCs derived from either sham or denervated (Den) femurs and transplanted in competition with young BM competitor cells (n=4 sham, 6 denervated mice) (left) and 5 months after secondary transplantation of 3×10^6 bone marrow from primary recipients (right) **(d). (e)** Left, representative confocal z-stack projections of HSCs sorted from sham or denervated femurs and stained with Cdc42, Tubulin and DAPI. Scale bar, 10 μm. Right, quantification of the percentage of Cdc42 and Tubulin polarized HSCs out of total HSCs scored (total of 356 sham and 353 denervated HSCs isolated from 4 mice per group). **(f)** Left, representative confocal z-stack projections of HSCs sorted from either young, old, sham or denervated femurs and stained with γH2AX and DAPI. Scale bar, 10

μm. Right, quantification of the percentage of HSCs with γH2AX foci (calculated as the mean percentage of a total of 164 young, 247 old, 381 sham and 355 Denervated HSCs isolated from 3 young, 3 old and 4 denervated mice). **(g)** Left, confocal *z*-stack projection montages from the femurs of sham and denervated tibiae from *Nestin-GFP* mice stained for CD31$^+$/CD144$^+$ double positive vasculature and DAPI. Scale bar, 500 μm. Right, assessment of arteriolar segment length as assessed by quantification of the length of the Nestin-GFP^{bright} signal covering CD31$^+$ CD144$^+$ double-positive arteriole in sham and denervated tibiae (n=8 and 11 sham and denervated projections, respectively; 4 mice). **(h)** Left, representative gating strategy for FACS quantification and sorting of MSCs (CD45$^-$ Ter119$^-$ CD31$^-$ CD51$^+$ PDGFRα$^+$) in sham (top) and denervated (bottom) femurs. Right, quantification of MSCs isolated from sham and denervated femurs from denervated mice (n=6 mice). **(i)** Frequency of CFU-F from sorted MSCs from denervated femurs, plated at equal numbers at clonal densities under CFU-F culture conditions (n=4 mice). **(j)** Quantification of mRNA levels of *Cxcl12, Scf, Angpt1* and *Vcam1* relative to *Gapdh* in sorted MSCs derived from sham and denervated tibia (normalized to sham; n=6 mice). Data represented as mean ± s.e.m., *p* value determined by two-tailed paired *t*-test (**b**, **h**–**j**) and two-tailed unpaired *t*-test (**c**–**g**).
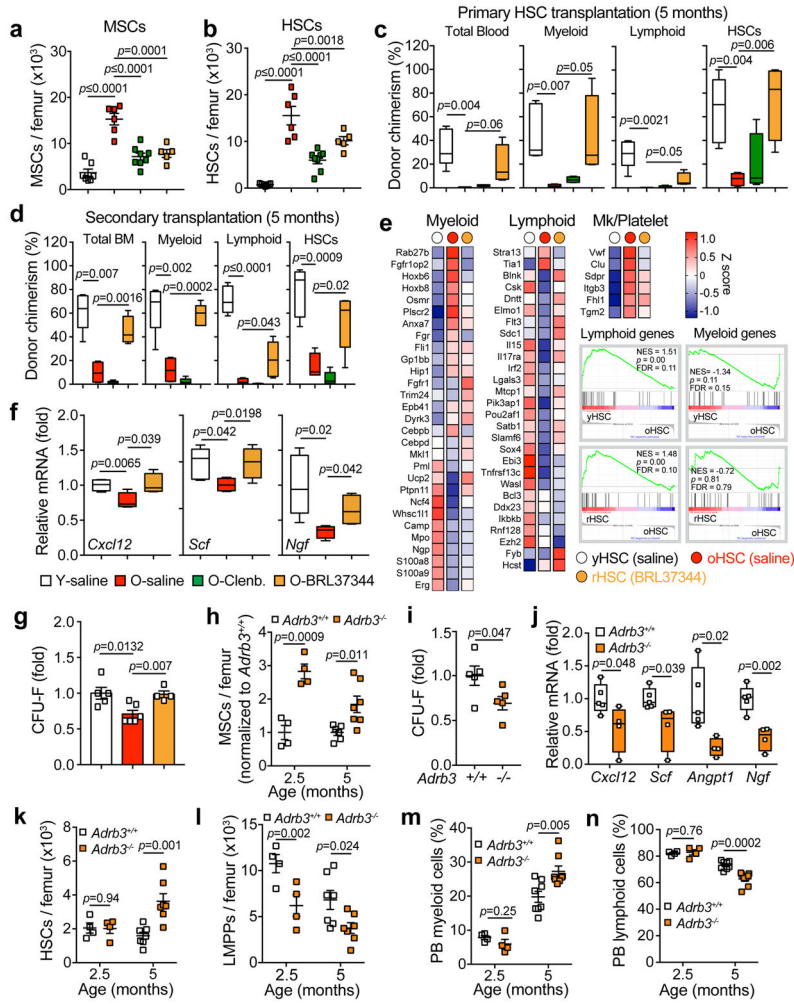
Figure 5. ADRβ3 signaling is essential for maintenance of aging HSCs

(a, b) Absolute numbers of MSCs (CD45$^-$ Ter119$^-$ CD31$^-$ CD51$^+$ PDGFRα$^+$) (a) and HSCs (lineage$^-$ Sca-1$^+$ c-Kit$^+$ CD48$^-$ CD150$^+$) (b) in young and old mice implanted with osmotic pumps containing either saline, the β2-adrenergic agonist clenbuterol or the β3-adrenergic agonist BRL37344 (n=7 young-saline, 6 old-saline, 8 old-clenbuterol and 5 old-BRL37344 mice). (c) Total blood chimerism (CD45.2$^+$), blood myeloid chimerism (Mac-1$^+$ CD45.2$^+$), blood lymphoid chimerism (B220$^+$ CD4$^+$ CD8$^+$ CD45.2$^+$) and HSC chimerism (lineage$^-$ Sca-1$^+$ c-Kit$^+$ CD48$^-$ CD150$^+$ CD45.2$^+$) in CD45.1 recipient mice transplanted with 200 HSCs, derived from the mice described in **a** and **b**, at 5 months after transplantation. (n= 5 young-saline, 4 old-saline, 4 old-clenbuterol and 4 old-BRL37344 mice). (d) Bone marrow chimerism following secondary bone marrow transplantation from the mice described in **c**, 5 months after transplantation. (n=5 young-saline, 4 old-saline, 5 old-clenbuterol and 5 old-BRL37344 mice). (e) Heat map of mean gene expression levels in young HSCs (yHSCs), old HSCs (oHSCs) and BRL37344 rejuvenated HSCs (rHSCs) (n=3 samples per group) of selected myeloid, lymphoid and megakaryocyte/platelet lineage genes and signature enrichment plots from GSEA using myeloid and lymphoid signature gene sets[11]. Shown are the Normalized Enrichment Score (NES), *p*-value and false discovery rate

(FDR) of the enrichment. **(f)** Quantification of mRNA levels of *Cxcl12, Scf* and *Ngf* relative to *Actb* in sorted MSCs derived from mice described in (**a**–**b**) (n=5 young-saline, 4 old-saline and 4 old-BRL37344; normalized to young-saline). **(g)** CFU-F frequency from sorted MSCs derived from mice described in **a** and **b** (normalized to young-saline; n=5 young-saline, 6 old-saline and 4 old-BRL37344 mice). **(h)** Absolute numbers of MSCs from *Adrb3*$^{+/+}$ and *Adrb3*$^{-/-}$ mice at 2.5 and 5 months of age (normalized to *Adrb3*$^{+/+}$; n=4 mice per 2.5-month group, 6 *Adrb3*$^{+/+}$, 7 *Adrb3*$^{-/-}$ per 5 month group). **(i, j)** CFU-F frequency from sorted MSCs (normalized to *Adrb3*$^{+/+}$; n=5 mice per group) **(i)** and quantification of mRNA levels of *Cxcl12, Scf, Angpt1* and *Ngf* relative to *Gapdh* in sorted MSCs (normalized to *Adrb3*$^{+/+}$; n=5 and 4 *Adrb3*$^{+/+}$ and *Adrb3*$^{-/-}$ mice respectively) **(j)** from 2.5 month old *Adrb3*$^{+/+}$ and *Adrb3*$^{-/-}$ mice. **(k–n)** Absolute numbers of HSCs **(k)**, LMPPs (lineage^{-} Sca-1^{+} c-Kit^{+} CD34^{+} Flt3^{+}) **(l)**, peripheral blood (PB) myeloid cells (Mac-1^{+} Gr-1^{+}) **(m)** and lymphoid cells (B220^{+} CD4^{+} CD8^{+}) cells **(n)** in *Adrb3*$^{+/+}$ and *Adrb3*$^{-/-}$ mice at 2.5 and 5 months of age (n=4 mice per 2.5-month group, 7 (**k**–**i**) and 8 (**m**–**n**) per 5 month group). Data represented as mean ± s.e.m, *p* value determined by two-tailed *t*-test. For box plots, the box spans from the 25th to 75th percentiles and the centerline is plotted at the median. Whiskers represent minimum to maximum range.